

## PAPER

[View Article Online](#)  
[View Journal](#) | [View Issue](#)Cite this: *J. Mater. Chem. C*, 2021,  
9, 8650

# Nucleation management for the ambient fabrication of high-performance perovskite photodetectors with the eco-friendly *tert*-butanol anti-solvent†

Xin Tang,<sup>‡</sup> Tengteng Li,<sup>‡</sup> Qingyan Li,<sup>‡</sup> Hongliang Zhao,<sup>‡</sup> Silei Wang,  
Mengyao Li, Xuanruo Hao, Yating Zhang<sup>‡</sup>\* and Jianquan Yao<sup>\*</sup>

The preparation of most high-performance perovskite optoelectronic devices usually relies on costly inert or vacuum conditions to circumvent the inimical effects of moisture, which could lead to inferior crystallization processes and nonuniform morphology. Hence, it is imperative to develop a reliable and cost-effective approach to deposit a high-quality perovskite in ambient air. Herein, we investigated the influence of *tert*-butanol (TBA), *sec*-butanol (SBA), and isobutanol (IBA) on the nucleation mechanism in ambient atmosphere. It was found that TBA as an eco-friendly anti-solvent leads to the formation of uniform, smooth, pinhole-free, mirror-like perovskite films with enhanced optoelectronic properties compared with other solvents. More excitingly, perovskite photodetectors fabricated using TBA exhibited an excellent photoresponsivity of  $1.93 \text{ A W}^{-1}$ , which is among the highest values reported for the same device structure and also demonstrates the distinctive advantages of our nucleation management strategy. This work sheds light on developing high-performance perovskite photodetectors using eco-friendly solutions in ambient environment.

Received 14th April 2021,  
Accepted 3rd June 2021

DOI: 10.1039/d1tc01726h

[rsc.li/materials-c](https://rsc.li/materials-c)

## Introduction

Photodetectors (PDs) play an indispensable role in many optoelectronic applications, including optical communication, biochemical detection, machine vision, and image sensing.<sup>1–5</sup> Until now, most of the high-performance commercial PDs have been mainly based on conventional inorganic semiconductor materials such as Si, InGaAs, and GaN,<sup>6–8</sup> which are costly, complex, and time-consuming to fabricate. In recent years, solution-processed organic–inorganic hybrid perovskite (OIHP) materials have emerged, which show huge application potential in solar cells, light-emitting diodes, and PDs.<sup>9–14</sup> Due to their distinctive optoelectronic properties, including high optical absorption coefficients in the ultraviolet–near-infrared region, long exciton diffusion lengths, high charge carrier mobility, and tunable bandgaps, OIHPs are considered promising candidates for constructing high-performance PDs.<sup>15–19</sup> Compared to the traditional PDs, Perovskite PDs (PPDs) have the appealing advantages of low cost, convenient

operation, and flexibility.<sup>20</sup> Nevertheless, there is still a certain extent of resistance in the mass production and practical application of OIHPs, involving the degradation of the material itself, special preparation environment, *etc.* As the organic cation in perovskites is quite sensitive to light, humidity, and temperature in ambient air, the processing environment for most high-performance perovskite optoelectronic devices is typically in a nitrogen ( $\text{N}_2$ )-filled glovebox with a humidity less than  $<1\%$  and/or vacuum deposition machines, which enormously increases the cost of device manufacturing and equipment maintenance.<sup>21,22</sup> Clearly, it is imperative to fabricate high-quality perovskite films under ambient conditions without special precautions.

Numerous previous studies have shown that the morphology and crystalline quality of perovskite films are crucial for achieving high-performance devices.<sup>23–26</sup> High-quality perovskite films guarantee sufficient light absorption, efficient charge transport, and reduced recombination. To fabricate high-quality ambient processed perovskite films, several alternative approaches have been proposed, such as composition engineering, additive engineering, solvent engineering, interface engineering, and other methods.<sup>27–34</sup> Among the solvent engineering methods, the anti-solvent assisted crystallization method has become the preference for exploring the preparation of high-quality perovskites in ambient air due to its simplicity,

Key Laboratory of Opto-Electronics Information Technology, Ministry of Education, School of Precision Instruments and Opto-Electronics Engineering, Tianjin University, Tianjin 300072, China. E-mail: [yating@tju.edu.cn](mailto:yating@tju.edu.cn)

† Electronic supplementary information (ESI) available. See DOI: 10.1039/d1tc01726h

‡ These authors contributed equally to this work.



scalability, and low cost.<sup>35</sup> Normally, ideal anti-solvents with low boiling point, polarity, and solubility of perovskite can significantly reduce the solubility of perovskites in the precursor and accelerate its nucleation to generate perovskite crystal seeds, thus inducing a high-quality perovskite thin film with a high surface coverage, a large grain size, and a low defect concentration.<sup>36</sup> Although many anti-solvents, including chlorobenzene (CB),<sup>37</sup> toluene (TL),<sup>38</sup> isopropanol acetate (IPA),<sup>39</sup> and acetate-based solvents,<sup>40</sup> are considered as competitive candidates for solvent engineering, a majority of them are carcinogenic and easily cause irreversible harm to human health.<sup>41,42</sup> More importantly, air-processed perovskite films prepared using the ordinary anti-solvents are often accompanied by varying degrees of pinholes and rough surface morphology, which will lead to perceptibly inferior optoelectronic properties of OIHP films. Consequently, it is a challenge to develop a green anti-solvent that can effectively control the film-forming dynamics and quality of OIHP films in ambient air.

Herein, *tert*-butanol (TBA), *sec*-butyl alcohol (SBA), and iso-butanol (IBA) were used as the anti-solvents for preparing CH<sub>3</sub>NH<sub>3</sub>PbI<sub>3</sub> (MAPbI<sub>3</sub>) perovskite films in ambient air [relative humidity (RH) of 10–30%]. It was speculated that TBA, an eco-friendly tertiary alkyl alcohol, could prevent moisture from influencing nucleation and could produce a high-quality perovskite film with a more uniform, smooth, pinhole-free, mirror-like surface morphology. Upon optimization, the PDs processed using TBA exhibited a high photoresponsivity of nearly 1.93 A W<sup>-1</sup> under illumination using a 532 nm laser at a -2 V bias voltage, and a high detectivity of over 7.62 × 10<sup>11</sup> Jones with a linear dynamic range of 104 dB. It is expected that this study would open a new avenue for the fabrication of state-of-the-art OIHP PDs in ambient air and uncontrolled laboratory conditions, potentially enabling the commercialization of devices. More significantly, the strategy of using TBA for nucleation management provides a green alternative for the ambient fabrication of high-performance PPDs.

## Experimental

### Materials and methods

Lead iodide (PbI<sub>2</sub>, >99.99%), methylammonium iodide (MAI, CH<sub>3</sub>NH<sub>3</sub>I, >99.5%), poly(3,4-ethylenedioxythiophene):polystyrene sulfonate (PEDOT:PSS), phenyl-C61-butyric acid methyl ester (PC<sub>61</sub>BM, >99%), and 4,7-diphenyl-1,10-phenanthroline (BCP, Bphen, >99%) were all purchased from Xi'an Polymer Light Technology Corp. Dimethyl formamide (DMF, 99.5%), dimethylsulfoxide (DMSO, 99.5%), *tert*-butanol (TBA), *sec*-butanol (SBA), and iso-butanol (IBA) were all purchased from Aladdin. All chemicals were used without further purification.

### Device fabrication

All devices in this study were based on ITO-coated glass substrates. The substrates were sequentially cleaned with detergent, ultrahigh purified water, acetone, and isopropanol, and then post-treated with an ultraviolet ozone cleaner for 15 min.

The PEDOT:PSS solution was spin-coated on top of the cleaned ITO substrates at 4000 rpm for 40 s and then continuously annealed at 150 °C for 15 min. The perovskite precursor solution was prepared by dissolving PbI<sub>2</sub> and MAI with a molar ratio of 1:1.05 in the mixed solvent of DMSO and DMF with a volume ratio of 1:9 and stirring overnight at 25 °C. All anti-solvents were heated at 35 °C for 20 min before dropping. Then, 100 μL perovskite precursor solution was deposited onto the PEDOT:PSS substrate at 6000 rpm for 30 s and 265 μL of the anti-solvent was dropped on the wet film at about the 7th second during the spin-coating process. All the spin-coating processes mentioned above were implemented in the ambient atmosphere (RH of 10–30%). Subsequently, the samples were rapidly transferred to a hot plate, first annealed in ambient air at 100 °C for 20 min, and then annealed in a DMSO atmosphere at 100 °C for 10 min. Next, a chlorobenzene solution of PC<sub>61</sub>BM (20 mg mL<sup>-1</sup>) and an ethanol solution of BCP (0.7 mg mL<sup>-1</sup>) were successively spin-coated on the perovskite film at 3000 rpm and 6000 rpm, respectively. Finally, the devices were completed by evaporating an 80 nm-thick Ag electrode.

### Measurement and characterization

The surface morphologies of the different perovskite films were characterized using SEM (GeminiSEM 500, Germany) and AFM (CSPM5500, China). The absorption of perovskite films processed using different anti-solvents was measured using a Shimadzu UV-2600 (Japan). The X-ray diffraction (XRD) measurement of perovskite films was performed using a D8 ADVANCE (Germany). FTIR microspectroscopy was carried out using a fluorescence spectrophotometer (Nicolet IN10, Britain). The *I*-*V* characteristics of all PDs under 450 nm, 532 nm, and 808 nm laser illumination were measured using a Keithley 2400 source meter instrument.

## Results and discussion

Fig. S1 (ESI†) presents the schematic diagram of the device and the energy level diagram of PPDs. ITO and Ag were used as the anode and cathode, respectively. Herein, the ITO electrode with a work function of -4.7 eV and the Ag electrode with a work function of -4.3 eV were used as the cathode and anode in this PPD, respectively. The perovskite light-absorbing layer was sandwiched between the PEDOT:PSS and PC<sub>61</sub>BM/BCP layers, which can collect and transport the holes and electrons, respectively. In particular, the strictly matched electron and hole transport in Fig. S1b (ESI†) ensures effective carrier separation and extraction, further ensuring the successful operation of the photodetector. Fig. 1a shows the schematic diagram of the fabrication process of the MAPbI<sub>3</sub> film. Generally, the formation of perovskite thin films deposited using the anti-solvent assisted crystallization method mainly involves two critical stages: (a) the nucleation of the MAI·PbI<sub>2</sub>·DMSO intermediate phase in the spin-coating process induced by solvent evaporation and anti-solvent addition; (b) conversion of the MAI·PbI<sub>2</sub>·DMSO intermediate phase to perovskite and



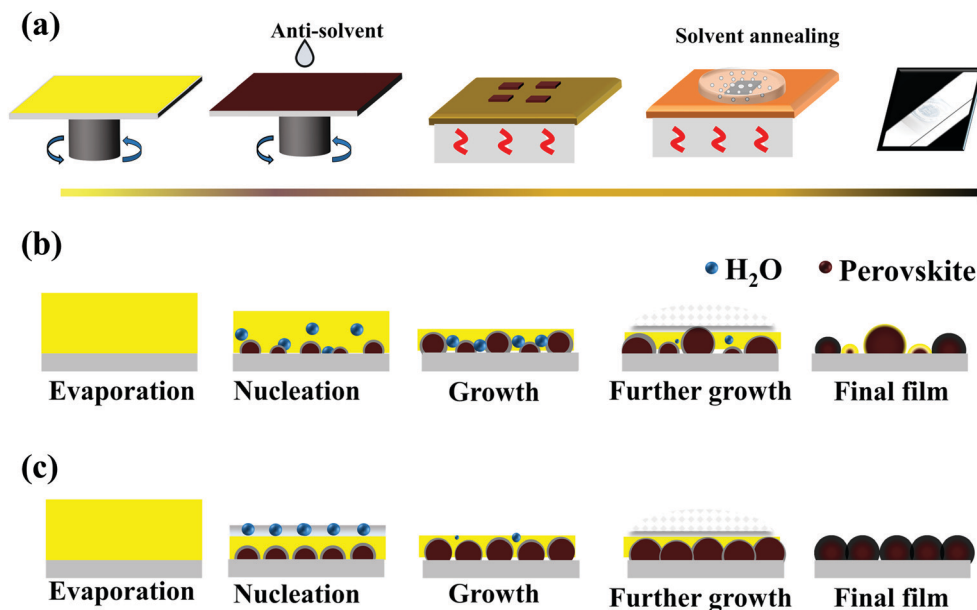


**Fig. 1** (a) Schematic illustration of the anti-solvent assisted crystallization process for fabricating perovskite films. (b) Model of the nucleation/growth competition of the perovskite crystal grown from the precursor solution using ordinary anti-solvents in ambient air. (c) Model of the nucleation/growth competition of the perovskite crystal grown from the precursor solution using the TBA anti-solvent in ambient air.

the crystal growth of the perovskite in the annealing stage. In the above nucleation process, the properties of the anti-solvents, such as vapor pressure, boiling point, and polarity, play a vital role in determining the film formation quality. Indeed, the introduction of high vapor pressure and low boiling point anti-solvents can significantly accelerate the evaporation of excess DMF solvent and produce local supersaturation conditions to accelerate the nucleation, further promoting the uniformity and high quality of the film.<sup>40,43</sup> Simultaneously, the polarity of the anti-solvent also influences the coordination ability of the solvent, which greatly determines the nucleation and growth of the perovskite crystals. Since low dipole moments lead to the formation of intermediate phases and result in larger grains, a low-polarity anti-solvent tends to facilitate the first stage in the crystallization process.<sup>43</sup> Furthermore, as shown in Fig. 1b, considering that the perovskite film is sensitive to the moisture in the air, ordinary anti-solvents without special treatment will inevitably introduce moisture in the intermediate phase, which could cause serious potential hazards for the subsequent crystal growth and even accelerate

the degradation process of perovskite crystals. In contrast, as illustrated in Fig. 1c, since airborne moisture preferentially forms solutions with the anti-solvents rather than reacting with the perovskite intermediate phase, the introduction of more water-soluble anti-solvents can serve to protect the intermediate phase from the negative impact of moisture.<sup>40</sup> The subsequent annealing stage, especially the solvent annealing treatment, will further improve the morphology of the perovskite films and promote grain growth.

Based on the physical properties of TBA, SBA and IBA mentioned in Table 1, we found that TBA has the relatively highest vapor pressure ( $46.0 \pm 0.3$  mmHg), lowest boiling point ( $84.6 \pm 8.0$  °C), lowest polarity (0.389), and optimal water solubility. These properties favor TBA anti-solvent assisted perovskite nucleation in the air for the following reasons: (1) the high vapor pressure and low boiling point greatly accelerate the evaporation of excess DMF; (2) the low polarity facilitates rapid nucleation and formation of the adduct  $\text{MAI-PbI}_2\cdot\text{DMSO}$ ; (3) the high water solubility reduces the impact of moisture in the intermediate phase during the spin coating process. Moreover, TBA is an eco-friendly solvent with low toxicity and almost harmless to the human body and environment. Thus, it is reasonable to believe that TBA is an ideal anti-solvent for the preparation of a high-quality perovskite film in ambient air.

The nucleation effect of the  $\text{MAI-PbI}_2\cdot\text{DMSO}$  intermediate phase with different butanol-based anti-solvents was investigated by Fourier transform infrared (FTIR) spectroscopy. Fig. 2a shows FTIR spectra of the unannealed  $\text{MAPbI}_3$  films prepared using different anti-solvents (TBA, SBA, and IBA), which displayed similar absorbance peak positions. All the unannealed films exhibited N–H vibration peaks at approximately  $3200\text{ cm}^{-1}$  (green line) and S=O stretching at around  $1020\text{ cm}^{-1}$  attributed to

**Table 1** Physical properties (3D structure, vapor pressure, boiling point, polarity, and solubility in water) of solvents

Solvent	3D structure	Vapor pressure at 25 °C (mmHg)	Boiling point (°C)	Polarity	Solubility in H <sub>2</sub> O (g/100 mL)
TBA		$46.0 \pm 0.3$	$84.6 \pm 8.0$	0.389	Soluble
SBA		$25.2 \pm 0.3$	$96.6 \pm 3.0$	0.506	12.5
IBA		$16.4 \pm 0.4$	$105.0 \pm 8.0$	0.552	9.5



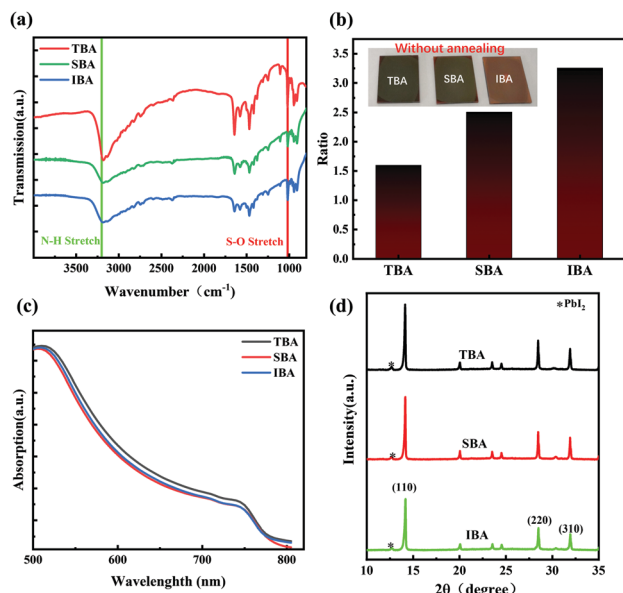


**Fig. 2** (a) FTIR spectra of the MAPbI<sub>3</sub> perovskite prepared using TBA, SBA, and IBA without annealing. (b) The ratio of the absorbance intensity of the unannealed perovskite films at 1020 and 3200 cm<sup>-1</sup> (1020 cm<sup>-1</sup>: 3200 cm<sup>-1</sup>). The appearance of the unannealed perovskite films prepared with the anti-solvent (inset). (c) UV-vis absorption spectra of the MAPbI<sub>3</sub> perovskite prepared using TBA, SBA, and IBA solvents with the annealing process. (d) XRD patterns of MAPbI<sub>3</sub> films on ITO substrates prepared using different anti-solvents.

DMSO (red line).<sup>44</sup> By comparing the ratio of absorbance at 1020 cm<sup>-1</sup> to the absorbance at 3200 cm<sup>-1</sup>, the concentration of DMSO in the intermediate phase could be inferred indirectly. From the results of this ratio (Fig. 2b), it was found that the DMSO content increased sequentially from TBA-treated perovskite (TBA-PVK), through SBA-treated perovskite (SBA-PVK) to IBA treated perovskite (IBA-PVK). The low ratio indicated few intermediate phases of MAI·PbI<sub>2</sub>·DMSO, which means the speed-up of the perovskite formation process.<sup>45</sup> Typically, the intermediate phase of MAI·PbI<sub>2</sub>·DMSO is detrimental because of the slow release of DMSO from the spin-coated intermediate film, which results in a poor-quality MAPbI<sub>3</sub> film.<sup>46</sup> Moreover, Fig. S2a (ESI<sup>†</sup>) and Fig. 2b show the morphology of the fresh perovskite film with and without annealing using different anti-solvents, respectively.<sup>47</sup> The color of the unannealed films was found to gradually change from dark brown (TBA-PVK) to yellowish brown (IBA-PVK), which implies that the content of DMSO in mesophase films increased. The results are well consistent with the observations from the FTIR spectra. In addition, compared with the annealed films in Fig. S2b (ESI<sup>†</sup>), the characteristic peak of DMSO disappeared, which indicates that the intermediate state of perovskite had transformed in the crystal growth process. Moreover, when 1% vol of deionized water was added to the anti-solvents, the intermediate phase of the TBA-PVK remained nearly invariable, while those of the others with less water-solubility decreased obviously (Fig. S3c and d, ESI<sup>†</sup>), further demonstrating the advantage of more water-soluble anti-solvents in the ambient fabrication of perovskites.

The UV-visible absorption spectra (range from 500 nm to 800 nm) of the perovskite films prepared with different

anti-solvents were measured, as shown in Fig. 2c. The absorption spectra of MAPbI<sub>3</sub> films are similar with an absorption edge of  $\approx 770$  nm. Yet, it is also obvious that the absorption of TBA-PVK is slightly larger than those of the films fabricated using pure SBA and IBA anti-solvents. This illustrates that the TBA anti-solvent improved the optical absorption characteristics of the perovskite films.

To further elucidate the influence of different anti-solvents on the crystallization of the perovskite films, the X-ray diffraction (XRD) patterns of the three perovskite films deposited on the ITO substrate were investigated (Fig. 2d). The typical strong diffraction peaks located at 14.12°, 28.44° and 31.88° for the 2 $\theta$  scan were observed, corresponding to the crystal planes of (110), (220) and (310), respectively, which were in good agreement with previous reports.<sup>25</sup> The results confirmed that the films are highly crystallized perovskite phases. Simultaneously, a weak diffraction pattern of PbI<sub>2</sub> appeared at 12.7° as shown in Fig. 2d. We speculate that the residual content of PbI<sub>2</sub> could be related to the different solubilities of PbI<sub>2</sub> and MAI compounds in various anti-solvents.<sup>48</sup>

To investigate the influence of the three butanol-based anti-solvents on the film morphology, top-view scanning electron microscopy (SEM) (Fig. 3a–c and j–l) and atomic force microscopy (AFM) measurements (Fig. 3g–i) were conducted on the prepared perovskite films. The TBA-PVK films exhibited an extremely homogeneous, smooth, pinhole-free polycrystalline morphology, which is shown in Fig. 3a and j. In particular, the average grain size of TBA-PVK was about 410.9 nm, which is significantly larger than those of the other films in Fig. 3d.

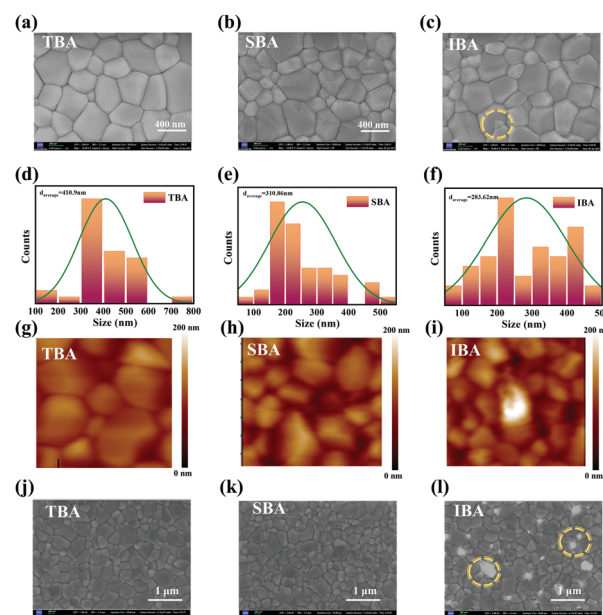


**Fig. 3** (a–c) Top-view SEM images of (a) TBA-PVK, (b) SBA-PVK, and (c) IBA-PVK films; the scale bar is 400 nm. (d–f) Grain-size distribution histograms of (d) TBA-PVK, (e) SBA-PVK, and (f) IBA-PVK films. (g–i) AFM images of (g) TBA-PVK, (h) SBA-PVK, and (i) IBA-PVK films. The scanning range of the images is 1  $\mu\text{m} \times 1 \mu\text{m}$ . (j–l) Top-view SEM images of (j) TBA-PVK, (k) SBA-PVK, and (l) IBA-PVK films; the scale bar is 1  $\mu\text{m}$ .





The SBA-PVK films became slightly inhomogeneous (Fig. 3b and k), and it could be observed from Fig. 3e that the average grain size decreases to 310 nm. In particular, the grain size in the IBA-PVK films became smaller and the presence of disordered overlapping coverage was exceedingly prominent (Fig. 3c). This result is in agreement with the image in Fig. 3l, where parts of the film (indicated by yellow dotted lines) appeared luminous. The grain size of the perovskite gradually increased, which may be related to the DMSO content in the intermediate perovskite phase.<sup>49</sup> Furthermore, the root mean square surface roughness values were measured to be 18.6, 21.5, and 23.9 nm for TBA-PVK, SBA-PVK, and IBA-PVK, respectively. TBA-PVK exhibited the relatively smoothest surface, which means fewer surface defect states and recombination. The 3D surface plot images (Fig. S3a, ESI†) also vividly confirm the variation of the surface roughness of perovskite films. In addition, to illustrate the effect of solvent annealing, the morphology characterization of perovskite films without solvent annealing has been added to Fig. S3b and c (ESI†).

The optoelectronic properties of the PPDs fabricated using different anti-solvents were measured under dark conditions and the illumination of a 532 nm laser. Fig. 4a shows the current variation of PDs processed using different anti-solvents with the change in applied bias voltage under the illumination of 1 mW cm<sup>-2</sup>. The dark current of TBA-treated perovskite PDs (TBA-PPDs) was significantly lower than those of the

SBA-treated perovskite PDs (SBA-PPDs) and IBA-treated perovskite PDs (IBA-PPDs) under negative bias. The photocurrent of TBA-PPD was also one order of magnitude higher than those of the other PDs under illumination, indicating that TBA is indeed a suitable anti-solvent that can markedly enhance the performance of PPDs. Specifically, the above results can be attributed to the fact the TBA-PVK film has better crystallization and morphological characteristics than the other films, which can effectually suppress the recombination loss caused by grain boundaries and intrinsic defects, thereby resulting in a lower dark current and a higher photocurrent. We further studied the dependence of the photocurrent on the light intensity of TBA-PPD. Fig. 4b displays the *I*-*V* curves under illumination using a 532 nm laser with different power densities. The results show that the photocurrent increased remarkably with the increase in power density. Particularly when the power density is 1000 μW cm<sup>-2</sup>, the photocurrent increases by nearly two orders of magnitude compared with the dark state, demonstrating that TBA-PPD has a satisfactory photocurrent response. To evaluate the advancement in the TBA-PPD, the responsivity (*R*) is also calculated according to the equation:<sup>50</sup>

$$R = \frac{I_{\text{ill}} - I_{\text{dark}}}{AL_e} \quad (1)$$

where *I*<sub>ill</sub> and *I*<sub>dark</sub> represent the photocurrent and dark current, respectively, *A* is the active area (0.04 cm<sup>2</sup>), and *L<sub>e</sub>* is the incident

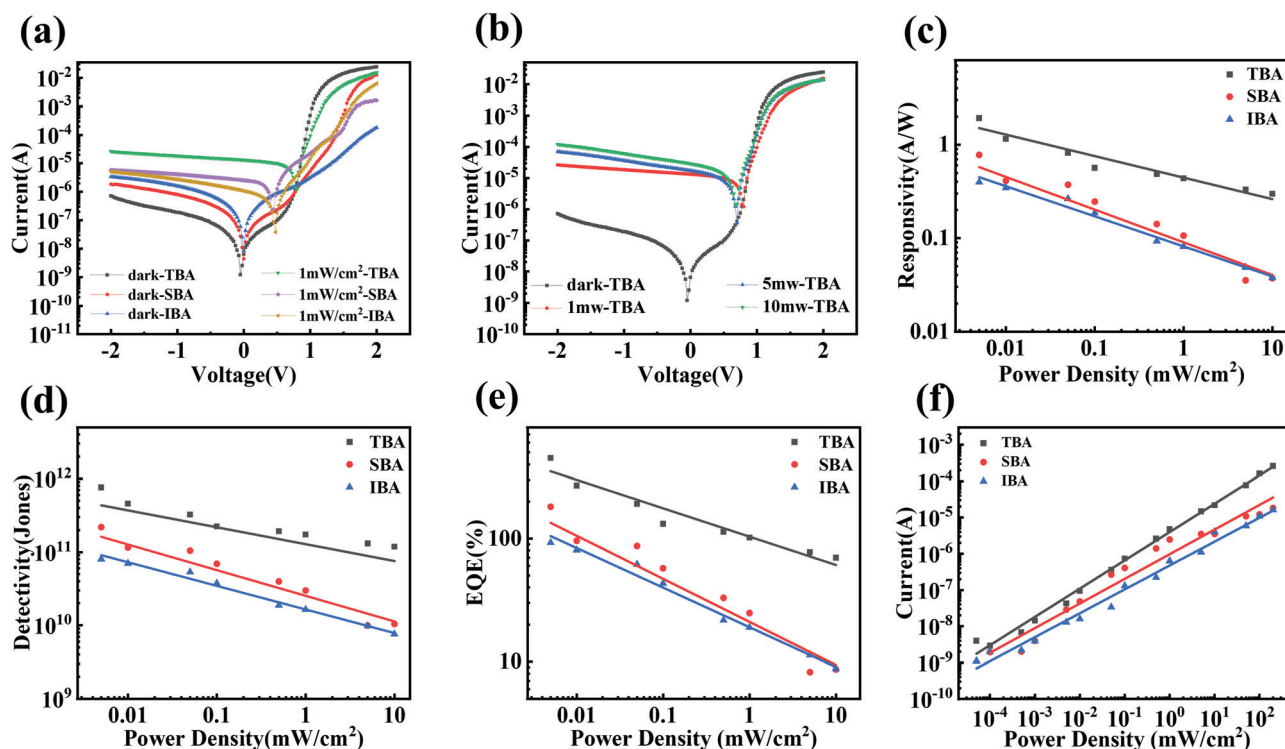


Fig. 4 Electrical properties of PPDs. (a) *I*-*V* characteristics of PDs treated using different anti-solvents under dark conditions and monochromatic illumination at a wavelength of 532 nm with a power density of 1 mW cm<sup>-2</sup>. (b) *I*-*V* characteristics of TBA-PPD under dark conditions and monochromatic illumination at a wavelength of 532 nm with different power densities. Dependences of (c) responsivity, (d) detectivity, and (e) EQE of PDs treated using different anti-solvents on the power densities under monochromatic illumination at a wavelength of 532 nm with a bias of -2 V. (f) LDR curves of PDs treated using different anti-solvents under monochromatic illumination at a wavelength of 532 nm with a bias of 0 V.



optical power density. Fig. 4c depicts the representative  $R$  in the device under an applied bias of  $-2$  V. Notably, under a weak illumination of  $5 \mu\text{W cm}^{-2}$ , the TBA-PPD shows excellent performance with an  $R$ -value of  $1.93 \text{ A W}^{-1}$ , which is the best responsivity among PPDs with identical vertical structures and a light-absorbing layer, even exceeding the responsivity of some devices prepared in a glove box environment. The  $R$ -value of SBA-PPD is  $0.78 \text{ A W}^{-1}$ , which is close to that of the ordinary PPD prepared under nitrogen protection. The  $R$  value of IBA-PPD is  $0.40 \text{ A W}^{-1}$ , which is the lowest among the three devices. Additionally, Table 2 summarizes the crucial performance parameters of the PPDs in this work and previously reported PPDs with similar vertical structures, using  $\text{MAPbI}_3$  perovskite as the single light absorber. Based on the  $R$  values, the specific detectivity ( $D^*$ ) of PPDs is further estimated according to the equation:<sup>51</sup>

$$D^* = R \cdot \sqrt{\frac{A}{2eI_{\text{dark}}}} \quad (2)$$

where  $I_{\text{dark}}$  is the dark current. With the increase in light power density,  $D^*$  shows a linear decreasing dependence. As shown in Fig. 4d, the calculated  $D^*$  values approaching  $7.62 \times 10^{11}$  Jones were achieved for the TBA-PPD under the illumination of  $5 \mu\text{W cm}^{-2}$ , which is much higher than that of PDs processed using SBA and IBA, corresponding to the  $D^*$  values of  $2.19 \times 10^{11}$  Jones and  $8.03 \times 10^{10}$  Jones, respectively. In addition to the responsivity, external quantum efficiency (EQE) is calculated by<sup>52</sup>

$$\text{EQE} = R \times \frac{hc}{e\lambda} \times 100\% \quad (3)$$

where  $h$  is Planck's constant,  $c$  is the velocity of incident light and  $\lambda$  represents the wavelength of the incident light. As described in Fig. 4e, the values of EQE exhibit a linear dependence on the power density of incident light similar to the  $R$  curves. A maximum EQE value of 450.04% is achieved by TBA-PPD, corresponding to a power density of  $5 \mu\text{W cm}^{-2}$  and a bias voltage of  $-2$  V. The EQE values of SBA-PPD and IBA-PPD are 181.74% and 92.71%, respectively, which are much lower than that of TBA-PPD.

The linear weak-light response range is customarily characterized by the linear dynamic range (LDR), defined by the following equation:<sup>53</sup>

$$\text{LDR} = 20 \log \frac{I_{\text{upper}} - I_{\text{dark}}}{I_{\text{lower}} - I_{\text{dark}}} \quad (4)$$

where  $I_{\text{upper}}$  and  $I_{\text{lower}}$  mean the upper and lower photocurrent values at which the current response deviates from linearity in a particular range, respectively. Fig. 4f shows the LDR values of PDs illuminated using a 532 nm laser with light intensities in the range from  $50 \text{ nW cm}^{-2}$  to  $190 \text{ mW cm}^{-2}$ . The photocurrent of TBA-PPD increases linearly at a dynamic light intensity ranging from  $100 \text{ nW cm}^{-2}$  to  $190 \text{ mW cm}^{-2}$  with a 532 nm laser. This result corresponds to a LDR value of 104 dB for the TBA-PPD. This linear response might have resulted from the excellent carrier transport properties of TBA-PVK and the low electron trap density in the whole photodetector. The LDR values of SBA-PPD and IBA-PPD are 72 dB and 71 dB, respectively.

To explore the instantaneous photoresponse time characteristics, the current–time ( $I$ – $T$ ) curves were measured at a 0 V bias under 532 nm laser irradiation with a light density of  $1 \text{ mW cm}^{-2}$  for TBA-PPDs, as shown in Fig. 5a. The device displays striking on–off stability and cycle repeatability, revealing the application potential of TBA-PPD in optical modulation switches. Besides, the corresponding photocurrent responses of SBA-PPD and IBA-PPD are shown in Fig. S5 and S6 (ESI†). To accurately evaluate the response times of the devices, we measured the response times of different PPDs under irradiation using a 532 nm pulse laser with a modulation frequency of 100 Hz. As illustrated in Fig. 5b, the rise time ( $t_{\text{rise}}$ ) and fall time ( $t_{\text{fall}}$ ) of TBA-PPD are 71  $\mu\text{s}$  and 770  $\mu\text{s}$ , respectively. The rise and fall times of SBA-PPD are 135  $\mu\text{s}$  and 2.56 ms (Fig. S5a, ESI†), while the corresponding ones for IBA-PPD are 1.29 ms and 3.58 ms, respectively (Fig. S6a, ESI†).

The instantaneous photocurrent measured under 532 nm laser irradiation increases significantly with the increase of power density in the range of  $0.5$  to  $10 \text{ mW cm}^{-2}$  (Fig. 5c). It can be seen from Fig. 4f and 5c that the photocurrent increases visibly with the increase in irradiation power, and the trend of both side curves is in agreement. The TBA-PPD can achieve an effective optical switch response under different power densities ranging from  $100 \text{ nW cm}^{-2}$  to  $190 \text{ mW cm}^{-2}$ . A similar growth trend of instantaneous photocurrent could also be observed with the 450 nm laser (Fig. S4a, ESI†) and 808 nm laser (Fig. S4b, ESI†) illuminations with different power densities, reflecting the excellent optical switch response characteristics of TBA-PPD, which is of great significance for its practical applications. The photocurrent responses of

Table 2 Performance parameters of PDs in this work and previously reported PDs with similar vertical structures

Device structure	Wavelength (nm)	Responsivity ( $\text{A W}^{-1}$ )	Detectivity (Jones)	Processing condition	Ref.
ITO/PEDOT:PSS/MAPbI <sub>3</sub> /PCBM/BCP/Al	500	0.87	$9.1 \times 10^{11}$	Inert gas protection	54
ITO/TiO <sub>2</sub> /PCBM/MAPbI <sub>3</sub> /P3HT/MoO <sub>3</sub> /Ag	500	0.34	$4.8 \times 10^{12}$	Inert gas protection	55
ITO/PEDOT:PSS/MAPbI <sub>3</sub> /PCBM/Al	670	0.314	—	Inert gas protection	56
ITO/PEDOT:PSS/MAPbI <sub>3</sub> /PCBM/AZO/Al	700	0.3	—	Inert gas protection	57
ITO/PEDOT:PSS/MAPbI <sub>3</sub> /PCBM/BCP/Ag	532	1.06	$1.48 \times 10^{11}$	Inert gas protection	58
FTO/TiO <sub>2</sub> /MAPbI <sub>3</sub> /Spiro/Au	660	0.18	$6.3 \times 10^{10}$	Inert gas protection	59
FTO/TiO <sub>2</sub> /Al <sub>2</sub> O <sub>3</sub> /PCBM/MAPbI <sub>3</sub> /Spiro/Au/Ag	600	0.4	$\sim 10^{12}$	Inert gas protection	60
ITO/NiOx/MAPbI <sub>3</sub> /PMMA/C <sub>70</sub> /BCP/Cu	400–800	0.1–0.5	$\sim 10^{11}$	Inert gas protection	61
ITO/PEDOT:PSS/MAPbI <sub>3</sub> /PCBM/BCP/Ag (TBA-PDs)	532	1.93	$7.62 \times 10^{11}$	Air conditions	This work
ITO/PEDOT:PSS/MAPbI <sub>3</sub> /PCBM/BCP/Ag (SBA-PDs)	532	0.78	$2.19 \times 10^{11}$	Air conditions	This work
ITO/PEDOT:PSS/MAPbI <sub>3</sub> /PCBM/BCP/Ag (IBA-PDs)	532	0.40	$8.03 \times 10^{10}$	Air conditions	This work



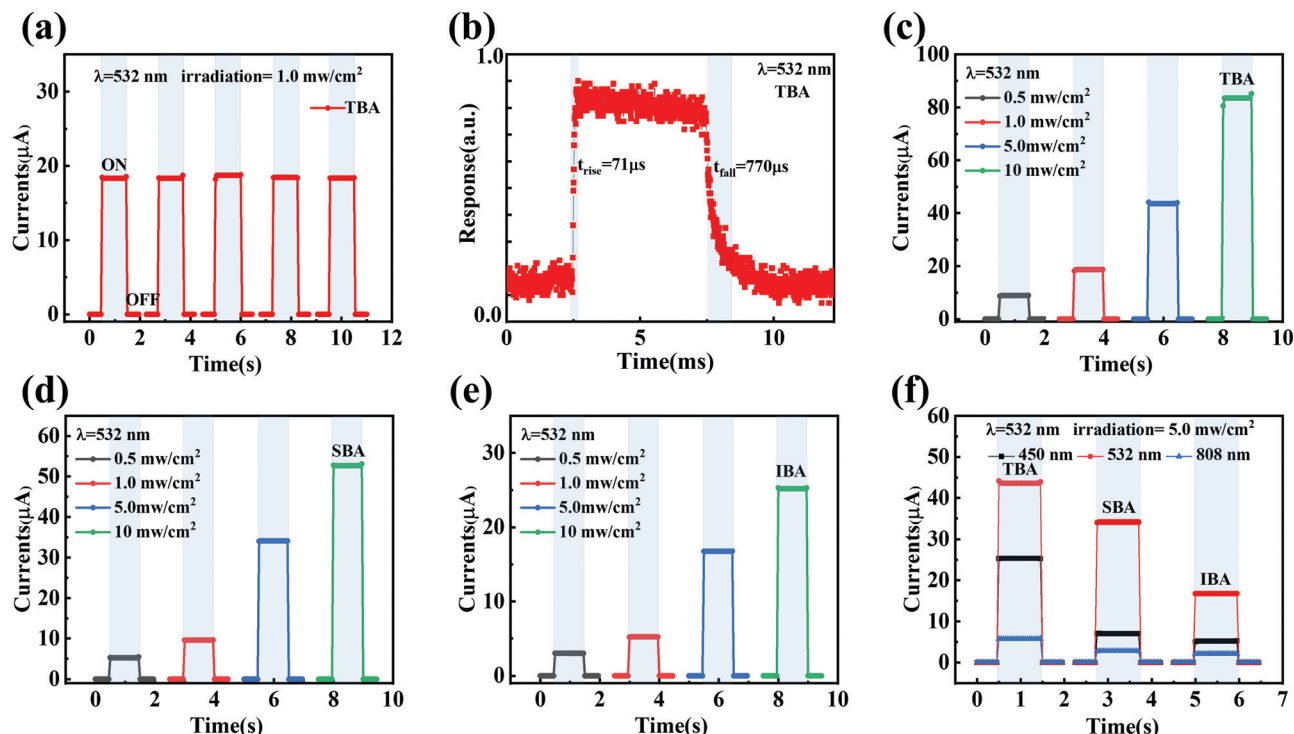


Fig. 5 (a) Photoswitching characteristics of the TBA-PPD under 532 nm light illumination as the light circulates on and off ( $1 \text{ mW cm}^{-2}$ ,  $V_{\text{Bias}} = 0 \text{ V}$ ). (b) Response time measurement under one on–off illumination cycle of a 532 nm laser with a pulse frequency of 100 Hz. (c–e) Photocurrent responses of TBA-PPD, SBA-PPD and IBA-PPD under 532 nm light illumination at different power densities, respectively. (f) Photocurrent response of PDs processed using different anti-solvents under 532, 450, and 808 nm light illumination with a power density of  $5 \text{ mW cm}^{-2}$ .

SBA-PPD and IBA-PPD under 450 and 808 nm laser illuminations at different power densities are presented in Fig. S5b, c and S6b, c (ESI†), respectively.

For further observation, we tested the photocurrents of the above three anti-solvent-treated PDs under 450, 532, and 808 nm laser illuminations with a specific incident power density of  $1 \text{ mW cm}^{-2}$  and a bias voltage of 0 V. Fig. 5f shows the light current response characteristics of three PPDs under laser illumination at different wavelengths. Interestingly, all PPDs displayed the weakest response intensity to the 808 nm laser and the most marked response intensity to the 532 nm laser, showing no difference from the absorption spectra, as plotted in Fig. 2c. Notably, regardless of the illumination wavelength, TBA-PPD showed the best photocurrent response. This also proves that TBA is more likely to avoid the influence of humidity in the air, facilitating nucleation and grain growth than SBA and IBA, to obtain perovskite films with good crystallinity and improved device performance. Furthermore, as depicted in Fig. S4c (ESI†), the histogram corresponding to the photocurrent response at the three illumination wavelengths more intuitively confirms this conclusion.

finding that, compared with SBA and IBA anti-solvents, the eco-friendly TBA could effectively reduce the influence of airborne moisture and improve the nucleation process, ultimately producing high-quality perovskite films with uniform, smooth, pinhole-free surface morphology. This TBA-optimized perovskite photodetector showed a high responsivity of  $1.93 \text{ A W}^{-1}$  under the illumination of a 532 nm laser with a power density of  $5 \mu\text{W cm}^{-2}$  at a bias voltage of  $-2 \text{ V}$ , a high detectivity of  $7.62 \times 10^{11} \text{ Jones}$ , and a large LDR of 104 dB. To the best of our knowledge, the responsivity performance of this photodetector is the highest among the same vertical device structures and even markedly exceeds some of the reported devices prepared in an inert atmosphere. Hence, it is believed that this study can provide an ideal green route for the fabrication of high-performance PPDs in ambient air and may pave the way for massive and low-cost manufacturing of PPDs.

## Conflicts of interest

There are no conflicts to declare.

## Acknowledgements

This work was supported by the National Natural Science Foundation of China (No. 61675147, 61735010, and 91838301), the National Key Research and Development

## Conclusions

In summary, we have demonstrated an effective anti-solvent-assisted nucleation management strategy for the ambient preparation of high-performance PPDs. We disclosed a key



Program of China (No. 2017YFA0700202), the Basic Research Program of Shenzhen (JCYJ20170412154447469), Beiyang Yong Junior Faculties of Tianjin University (No. 2019XRG-0056), the Innovation Projects of the Department of Education of Guangdong Province (2018KQNCX264) and Wenzhou City Governmental Public Industrial Technology Project (G20160014).

## References

- 1 Y. J. Fang, Q. F. Dong, Y. C. Shao, Y. B. Yuan and J. S. Huang, *Nat. Photonics*, 2015, **9**, 679–687.
- 2 F. P. García de Arquer, A. Armin, P. Meredith and E. H. Sargent, *Nat. Rev. Mater.*, 2017, **2**, 16100.
- 3 C. Bao, J. Yang, S. Bai, W. Xu, Z. Yan, Q. Xu, J. Liu, W. Zhang and F. Gao, *Adv. Mater.*, 2018, **30**, e1803422.
- 4 C. Li, J. Lu, Y. Zhao, L. Sun, G. Wang, Y. Ma, S. Zhang, J. Zhou, L. Shen and W. Huang, *Small*, 2019, **15**, e1903599.
- 5 J. Wang, S. Xiao, W. Qian, K. Zhang, J. Yu, X. W. Xu, G. P. Wang, S. Z. Zheng and S. H. Yang, *Adv. Mater.*, 2021, **33**, 9.
- 6 X. D. Qiu, X. G. Yu, S. Yuan, Y. H. Gao, X. M. Liu, Y. Xu and D. R. Yang, *Adv. Opt. Mater.*, 2018, **6**, 1700638.
- 7 I. Vurgaftman, J. R. Meyer and L. R. Ram-Mohan, *J. Appl. Phys.*, 2001, **89**, 5815–5875.
- 8 R. R. Zhuo, L. H. Zeng, H. Y. Yuan, D. Wu, Y. G. Wang, Z. F. Shi, T. T. Xu, Y. T. Tian, X. J. Li and Y. H. Tsang, *Nano Res.*, 2019, **12**, 183–189.
- 9 H. Cho, S. H. Jeong, M. H. Park, Y. H. Kim, C. Wolf, C. L. Lee, J. H. Heo, A. Sadhanala, N. Myoung, S. Yoo, S. H. Im, R. H. Friend and T. W. Lee, *Science*, 2015, **350**, 1222–1225.
- 10 Y. Li, Z. F. Shi, S. Li, L. Z. Lei, H. F. Ji, D. Wu, T. T. Xu, Y. T. Tian and X. J. Li, *J. Mater. Chem. C*, 2017, **5**, 8355–8360.
- 11 Y. Fang and J. Huang, *Adv. Mater.*, 2015, **27**, 2804–2810.
- 12 Q. Jiang, Y. Zhao, X. Zhang, X. Yang, Y. Chen, Z. Chu, Q. Ye, X. Li, Z. Yin and J. You, *Nat. Photonics*, 2019, **13**, 460–466.
- 13 Y. Li, Z. F. Shi, W. Q. Liang, L. T. Wang, S. Li, F. Zhang, Z. Z. Ma, Y. Wang, Y. Z. Tian, D. Wu, X. J. Li, Y. T. Zhang, C. X. Shan and X. S. Fang, *Mater. Horiz.*, 2020, **7**, 530–540.
- 14 Y. Li, Z. F. Shi, L. T. Wang, Y. C. Chen, W. Q. Liang, D. Wu, X. J. Li, Y. Zhang, C. X. Shan and X. S. Fang, *Mater. Horiz.*, 2020, **7**, 1613–1622.
- 15 M. Ahmadi, T. Wu and B. Hu, *Adv. Mater.*, 2017, **29**, 1605242.
- 16 L. Dou, Y. M. Yang, J. You, Z. Hong, W. H. Chang, G. Li and Y. Yang, *Nat. Commun.*, 2014, **5**, 5404.
- 17 W. Hu, R. S. Wu, S. Z. Yang, P. Fan, J. L. Yang and A. L. Pan, *J. Phys. D: Appl. Phys.*, 2017, **50**, 375101.
- 18 A. K. Jena, A. Kulkarni and T. Miyasaka, *Chem. Rev.*, 2019, **119**, 3036–3103.
- 19 L. Shen, Y. Fang, D. Wang, Y. Bai, Y. Deng, M. Wang, Y. Lu and J. Huang, *Adv. Mater.*, 2016, **28**, 10794–10800.
- 20 X. Hu, X. D. Zhang, L. Liang, J. Bao, S. Li, W. L. Yang and Y. Xie, *Adv. Funct. Mater.*, 2014, **24**, 7373–7380.
- 21 J. A. Christians, P. A. Miranda Herrera and P. V. Kamat, *J. Am. Chem. Soc.*, 2015, **137**, 1530–1538.
- 22 Y. Zhang, A. Kirs, F. Ambroz, C. T. Lin, A. S. R. Bati, I. P. Parkin, J. G. Shapter, M. Batmunkh and T. J. Macdonald, *Small Methods*, 2020, **5**, 2000744.
- 23 T. L. Bu, L. Wu, X. P. Liu, X. K. Yang, P. Zhou, X. X. Yu, T. S. Qin, J. J. Shi, S. Wang, S. S. Li, Z. L. Ku, Y. Peng, F. Z. Huang, Q. B. Meng, Y. B. Cheng and J. Zhong, *Adv. Energy Mater.*, 2017, **7**, 1700576.
- 24 H. Li, Y. Xia, C. Wang, G. Wang, Y. Chen, L. Guo, D. Luo and S. Wen, *ACS Appl. Mater. Interfaces*, 2019, **11**, 34989–34996.
- 25 Y. Yu, S. Yang, L. Lei, Q. Cao, J. Shao, S. Zhang and Y. Liu, *ACS Appl. Mater. Interfaces*, 2017, **9**, 3667–3676.
- 26 Y. Yun, F. Wang, H. Huang, Y. Fang, S. Liu, W. Huang, Z. Cheng, Y. Liu, Y. Cao, M. Gao, L. Zhu, L. Wang, T. Qin and W. Huang, *Adv. Mater.*, 2020, **32**, e1907123.
- 27 J. J. Duan, Z. Y. Liu, Y. F. Zhang, K. K. Liu, T. W. He, F. Wang, J. Dai and P. X. Zhou, *Opt. Mater.*, 2018, **85**, 55–60.
- 28 H. S. Ko, J. W. Lee and N. G. Park, *J. Mater. Chem. A*, 2015, **3**, 8808–8815.
- 29 L. Shi, H. Hao, J. Dong, T. Zhong, C. Zhang, J. Hao, J. Xing and H. Liu, *Nanomaterials*, 2019, **9**, 915.
- 30 R. Singh, S. Sandhu, H. Yadav and J. J. Lee, *ACS Appl. Mater. Interfaces*, 2019, **11**, 29941–29949.
- 31 J. Z. Song, J. H. Li, X. M. Li, L. M. Xu, Y. H. Dong and H. B. Zeng, *Adv. Mater.*, 2015, **27**, 7162–7167.
- 32 Y. Yang, T. Chen, D. Q. Pan, J. Gao, C. T. Zhu, F. Y. Lin, C. H. Zhou, Q. D. Tai, S. Xiao, Y. B. Yuan, Q. L. Dai, Y. B. Han, H. P. Xie and X. Y. Guo, *Nano Energy*, 2020, **67**, 104246.
- 33 X. M. Li, Y. Wu, S. L. Zhang, B. Cai, Y. Gu, J. Z. Song and H. B. Zeng, *Adv. Funct. Mater.*, 2016, **26**, 2435–2445.
- 34 J. W. Chen, J. Wang, X. B. Xu, J. H. Li, J. Z. Song, S. Lan, S. N. Liu, B. Cai, B. N. Han, J. T. Precht, D. Ginger and H. B. Zeng, *Nat. Photonics*, 2021, **15**, 9.
- 35 C. Hu, S. B. Shivarudraiah, H. H. Y. Sung, I. D. Williams, J. E. Halpert and S. H. Yang, *Sol. RRL*, 2021, 2000712, DOI: 10.1002/solr.202000712.
- 36 M. Xiao, L. Zhao, M. Geng, Y. Li, B. Dong, Z. Xu, L. Wan, W. Li and S. Wang, *Nanoscale*, 2018, **10**, 12141–12148.
- 37 J. W. Jung, S. T. Williams and A. K. Y. Jen, *RSC Adv.*, 2014, **4**, 62971–62977.
- 38 M. Yavari, M. Mazloum-Ardakani, S. Gholipour, M. M. Tavakoli, S. H. Turren-Cruz, N. Taghavinia, M. Gratzel, A. Hagfeldt and M. Saliba, *Adv. Energy Mater.*, 2018, **8**, 1800177.
- 39 P. Luo, W. Xia, S. Zhou, L. Sun, J. Cheng, C. Xu and Y. Lu, *J. Phys. Chem. Lett.*, 2016, **7**, 3603–3608.
- 40 F. Yang, G. Kapil, P. Zhang, Z. Hu, M. A. Kamarudin, T. Ma and S. Hayase, *ACS Appl. Mater. Interfaces*, 2018, **10**, 16482–16489.
- 41 C. Capello, U. Fischer and K. Hungerbühler, *Green Chem.*, 2007, **9**, 927–934.
- 42 D. Prat, J. Hayler and A. Wells, *Green Chem.*, 2014, **16**, 4546–4551.
- 43 S. Ghosh, S. Mishra and T. Singh, *Adv. Mater. Interfaces*, 2020, **7**, 2000950.





- 44 N. J. Jeon, J. H. Noh, Y. C. Kim, W. S. Yang, S. Ryu and S. I. Seok, *Nat. Mater.*, 2014, **13**, 897–903.
- 45 M. S. Yin, F. X. Xie, H. Chen, X. D. Yang, F. Ye, E. B. Bi, Y. Z. Wu, M. T. Cai and L. Y. Han, *J. Mater. Chem. A*, 2016, **4**, 8548–8553.
- 46 N. Ahn, D.-Y. Son, I.-H. Jang, S. M. Kang, M. Choi and N.-G. Park, *J. Am. Chem. Soc.*, 2015, **137**, 8696–8699.
- 47 Y. Bai, S. Xiao, C. Hu, T. Zhang, X. Y. Meng, Q. Li, Y. L. Yang, K. S. Wong, H. N. Chen and S. H. Yang, *Nano Energy*, 2017, **34**, 58–68.
- 48 Y. F. Wang, J. Wu, P. Zhang, D. T. Liu, T. Zhang, L. Ji, X. L. Gu, Z. D. Chen and S. B. Li, *Nano Energy*, 2017, **39**, 616–625.
- 49 M. Konstantakou, D. Perganti, P. Falaras and T. Stergiopoulos, *Crystals*, 2017, **7**, 291.
- 50 F. Li, C. Ma, H. Wang, W. Hu, W. Yu, A. D. Sheikh and T. Wu, *Nat. Commun.*, 2015, **6**, 8238.
- 51 F. G. Yan, Z. M. Wei, X. Wei, Q. S. Lv, W. K. Zhu and K. Y. Wang, *Small Methods*, 2018, **2**, 1700349.
- 52 Z.-Y. Peng, J.-L. Xu, J.-Y. Zhang, X. Gao and S.-D. Wang, *Adv. Mater. Interfaces*, 2018, **5**, 1870089.
- 53 H. Wang and D. H. Kim, *Chem. Soc. Rev.*, 2017, **46**, 5204–5236.
- 54 C. Liu, H. Peng, K. Wang, C. D. Wei, Z. X. Wang and X. Gong, *Nano Energy*, 2016, **30**, 27–35.
- 55 C. Liu, K. Wang, C. Yi, X. Shi, P. Du, A. W. Smith, A. Karim and X. Gong, *J. Mater. Chem. C*, 2015, **3**, 6600–6606.
- 56 C. Bao, W. Zhu, J. Yang, F. Li, S. Gu, Y. Wang, T. Yu, J. Zhu, Y. Zhou and Z. Zou, *ACS Appl. Mater. Interfaces*, 2016, **8**, 23868–23875.
- 57 X. Zhang, C. C. Liu, G. Ren, S. Y. Li, C. H. Bi, Q. Y. Hao and H. Liu, *Nanomaterials*, 2018, **8**, 318.
- 58 T. T. Li, Q. Y. Li, X. Tang, Z. L. Chen, Y. F. Li, H. L. Zhao, S. L. Wang, X. Ding, Y. T. Zhang and J. Q. Yao, *J. Phys. Chem. C*, 2021, **125**, 2850–2859.
- 59 H. Tao, H. Wang, Y. Bai, H. Zhao, Q. Fu, Z. Ma and H. Long, *J. Mater. Chem. C*, 2020, **8**, 6228–6235.
- 60 B. R. Sutherland, A. K. Johnston, A. H. Ip, J. Xu, V. Adinolfi, P. Kanjanaboos and E. H. Sargent, *ACS Photonics*, 2015, **2**, 1117–1123.
- 61 J. Peng, L. Cui, R. Li, Y. Xu, L. Jiang, Y. Li, W. Li, X. Tian and Q. Lin, *J. Mater. Chem. C*, 2019, **7**, 1859–1863.

